Reconstruction of Lamb wave dispersion curves by sparse representation with continuity constraints

Wenbo Zhao and Ming LiJoel B. HarleyYuanwei JinJosé M. F. Moura and Jimmy Zhu

Citation: The Journal of the Acoustical Society of America **141**, 749 (2017); doi: 10.1121/1.4974063
View online: http://dx.doi.org/10.1121/1.4974063
View Table of Contents: http://asa.scitation.org/toc/jas/141/2
Published by the Acoustical Society of America

Reconstruction of Lamb wave dispersion curves by sparse representation with continuity constraints

Wenbo Zhao[a] and Ming Li[b]
SYSU-CMU Joint Institute of Engineering, School of Electronics and Information Technology, Sun Yat-sen University, Xiaoguwei Island, Panyu District, Guangzhou, 510006, China

Joel B. Harley
Department of Electrical and Computer Engineering, University of Utah, 201 Presidents Circle, Salt Lake City, Utah 84112, USA

Yuanwei Jin
Department of Engineering and Aviation Sciences, University of Maryland Eastern Shore, 30925 College Backbone Road, Princess Anne, Maryland 21853, USA

José M. F. Moura and Jimmy Zhu
Department of Electrical and Computer Engineering, Carnegie Mellon University, 5000 Forbes Avenue, Pittsburgh, Pennsylvania 15213, USA

(Received 3 April 2016; revised 16 October 2016; accepted 30 December 2016; published online 3 February 2017)

Ultrasonic Lamb waves are a widely used research tool for nondestructive structural health monitoring. They travel long distances with little attenuation, enabling the interrogation of large areas. To analyze Lamb wave propagation data, it is often important to know precisely how they propagate. Yet, since wave propagation is influenced by many factors, including material properties, temperature, and other varying conditions, acquiring this knowledge is a significant challenge. In prior work, this information has been recovered by reconstructing Lamb wave dispersion curves with sparse wavenumber analysis. While effective, sparse wavenumber analysis requires a large number of sensors and is sensitive to noise in the data. In this paper, it extended and significantly improved by constraining the reconstructed dispersion curves to be continuous across frequencies. To enforce this constraint, it is included explicitly in a sparse optimization formulation, and by including in the reconstruction an edge detection step to remove outliers, and by using variational Bayesian Gaussian mixture models to predict missing values. The method is validated with simulation and experimental data. Significant improved performance is demonstrated over the original sparse wavenumber analysis approach in reconstructing the dispersion curves, in synthesizing noise-removed signals, in reducing the number of measurements, and in localizing damage. © *2017 Acoustical Society of America*.
[http://dx.doi.org/10.1121/1.4974063]

[ZHM] Pages: 749–763

I. INTRODUCTION AND BACKGROUND

Lamb waves are elastic waves that propagate in solid plates and are guided by the boundaries of the medium. Ultrasonic Lamb waves travel long distances with low attenuation,[1] making them well suited for remote nondestructive inspection and structural health monitoring of large plate-like structures.[2] Lamb waves are characterized by their dispersion curves, which describe the frequency-dependent phase and group velocity for each wave mode, as well as the frequency-dependent amplitude of each Lamb wave mode. While many Lamb wave techniques use approximated dispersion curve knowledge,[3–8] better knowledge of the dispersion curves and their amplitudes can yield significant improvement in applications.[9]

A. Overview of dispersion curves estimation

Due to their significance in Lamb wave analysis, there are many approaches for estimating the dispersion curves of Lamb waves. We divide these approaches into three categories: theoretical, numerical, and data-driven methods.

Dispersion curves can be theoretically computed by deriving the solution to the wave equation. For example, the dispersion curves for Lamb waves are defined by the Rayleigh-Lamb equation.[10,11] While theoretical modelling is often desired, it is limited to simple, isotropic

[a]Also at: Department of Electrical and Computer Engineering, Carnegie Mellon University, 5000 Forbes Avenue, Pittsburgh, PA 15213, USA.
[b]Also at: SYSU-CMU Shunde International Joint Research Institute, Eastern Nanguo Road, Shunde, 528300, China. Electronic mail: liming46@mail.sysu.edu.cn

structures[12,13] and requires impractically extensive and accurate knowledge about the structure and its environmental parameters.

Numerical simulations, such as the finite element method,[14–17] the semi-analytical finite element method,[17,18] and the scaled boundary finite element method,[19,20] allow us to analyze more complex structures. However, these approaches still require extensive structural and environmental knowledge[17] for the simulations to match experimental data.

Data-driven approaches use experimental data from real-world settings to extract or circumvent precise structural and environmental knowledge. These methods incorporate directly structural and environmental variations into their estimation procedure. Well-known data driven approaches include signal processing techniques[3–7] and machine learning methods.[21–26] Many signal processing techniques have limitations that reduce their effectiveness. For example, chirplet matching pursuit[5] removes valuable wideband frequency components and the zero-crossing technique[6] only examines certain modes of the dispersion curves. Machine learning methods require a significant amount of prior training data that is impractical to collect in many circumstances.

Sparse wavenumber analysis (SWA)[8,9] is a data-driven, model-aided approach that integrates experimental data with theoretical models and signal processing techniques to characterize the complex behavior of Lamb waves. Sparse wavenumber analysis reconstructs the frequency-wavenumber[27] dispersion curves and their complex amplitudes through the use of compressive sensing algorithms. Sparse wavenumber synthesis (SWS)[8] is then used to synthesize and predict the waveform as it propagates throughout the plate. When combined with matched field processing,[28] SWA and SWS can provide highly accurate target (i.e., structural defect or discontinuity) localization.[9]

While its effectiveness has been well demonstrated, SWA yields poor results when implemented with few sensors and noisy data. This is because SWA leverages very few assumptions about the dispersion curves. Specifically, it does not assume that the dispersion curves be continuous across frequency. In this paper, we significantly improve sparse wavenumber analysis by introducing a continuity constraint across frequencies. Our continuity constrained sparse wavenumber analysis (CCSWA) significantly improves the quality of the reconstruction of the dispersion curves and significantly reduces the number of measurements needed to accurately reconstruct them. This then leads to more accurate signal synthesis and much better damage localization results than existing alternatives.

B. Contributions of the paper

The contributions of this paper are threefold. First, we consider that the original SWA method[8] often produces fragmented reconstructed dispersion curves with missing data points. To address this limitation, we propose a new formulation of SWA that accounts explicitly for the continuity of the dispersion curves in the desired frequency range by introducing a continuity constraint regularization term in the sparsity-aware optimization cost function. Further, we add to the optimization algorithm a clustering step based on variational Bayesian Gaussian mixture models to restore missing points on the dispersion curves. By promoting better model fitting inside a dispersion curve cluster and promoting more sparsity outside of each cluster, we enforce continuity and more accurate dispersion curve reconstruction.

Second, we explicitly incorporate additive noise in the Lamb wave signal model. We assume that the additive noise has bounded energy without requiring a specific noise model. This enables us to account for a wide variety of noise sources in a real-world setting. This is different from prior signal models used by SWA (Refs. 8, 9, and 29) that do not consider noise. To remove the noise effectively, we develop an outlier detection step in the reconstruction of the continuity constrained dispersion curves.

Third, to reconstruct accurately the dispersion curves, we develop a comprehensive algorithm for our new formulation (with the continuity constraint and noise). The algorithm consists of six steps: basis pursuit, outlier detection, outlier removal, adaptive weight adjustment, variational Bayesian Gaussian mixture model clustering, and missing points restoring. We validate this algorithm with simulated and real-world experimental data. Unlike previous SWA results,[8] the reconstructed dispersion curves are continuous across frequencies and exhibit less "spike-like" noise. Furthermore, CCSWA achieves improved reconstruction accuracy with a significantly smaller number of measurements. As a result, CCSWA can synthesize more precise Lamb wave signals that are used for damage localization like in matched field processing or other applications.

C. Organization of the paper

The remainder of the paper is organized as follows. Section II, after briefly presenting the sparse representation of Lamb waves and the original SWA method,[8] introduces CCSWA and details the six-step algorithm to reconstruct continuity constrained dispersion curves. Using both basis pursuit[8] and orthogonal matching pursuit,[10,30–32] Sec. III compares CCSWA to SWA with simulation and experimental data. In Sec. IV, we draw conclusions.

II. CONTINUITY CONSTRAINED SPARSE WAVENUMBER ANALYSIS

In this section, we present CCSWA for reconstructing dispersion curves of Lamb waves. Section II A describes the Lamb waves signal model. Section II B introduces the continuity constrained convex optimization problem for sparse reconstruction. Finally, Sec. II C details the six-step algorithm that solves the CCSWA optimization problem.

A. Signal model

We choose cylindrical coordinates (r, θ, z), where the r-axis and the θ-axis represent the radial distance from the origin and the angle with respect to the reference direction on the plate, respectively. The z-axis is perpendicular to the plate. We consider piezoelectric sensors mounted on the

surface of the plate at position $z = z_0$. We assume an ideal impulse excitation source located at the origin. The response $H(r, \omega)$ at a receiving sensor at distance r from the transmitting source and at operating frequency ω is[8,33]

$$H(r,\omega) = \sum_{m=1}^{M} \sqrt{\frac{1}{k_m(\omega) r}} G_m(\omega) e^{j k_m(\omega) r}, \tag{1}$$

where $k_m(\omega)$ is the frequency dependent wavenumber of mode m, and G_m is the frequency dependent complex amplitude of mode m. The signal $H(r, \omega)$ is the superposition of M wave modes. Each mode is determined by its wavenumber $k_m(\omega)$ and the complex gain $G_m(\omega)$. To estimate the dispersion curves, we assume that data are collected from L sensors mounted on the plate under test. As a result, for each frequency ω, we obtain L sets of measurements

$$X(r_l, \omega) = H(r_l, \omega) S(\omega) + W(r_l, \omega), \quad l = 1, \ldots, L, \tag{2}$$

where the symbol $W(r_l, \omega)$ denotes additive measurement noise or interfering signals. The symbol $S(\omega)$ is the frequency spectrum of the excitation source. For the sake of simplicity, we assume $S(\omega) = 1$. Formulation (2) differs from the earlier work[8] by explicitly modeling the noise in the data. This enables us to develop estimation algorithms for dispersion curve reconstruction in the presence of noise and unwanted interference. Our goal is to estimate the M sets of unknown parameters $k_m(\omega)$ and $G_m(\omega)$ from L measurements. Next, we organize the measurement data into the vector

$$\mathbf{x}(\omega) = [X(r_1, \omega) \quad X(r_2, \omega) \cdots X(r_L, \omega)]^T. \tag{3}$$

As in prior work,[8] we assume $G_m(\omega)$ is a discrete sample of the continuous frequency-wavenumber spectrum $V(\kappa, \omega)$ at the wavenumber value $k_m(\omega)$, i.e.,

$$V(\kappa, \omega) = \begin{cases} G_m(\omega) & \text{if } \kappa = k_m(\omega) \text{ for some } m, \\ 0 & \text{otherwise.} \end{cases} \tag{4}$$

We now discretize κ across $N \gg L$ possible wavenumber values κ_n, $n = 1, \ldots, N$, and write the samples of $V(\kappa, \omega)$ at these N values as

$$\mathbf{v}(\omega) = [V(\kappa_1, \omega) \quad V(\kappa_2, \omega) \cdots V(\kappa_N, \omega)]^T. \tag{5}$$

The N values κ_n are finely sampled across the wavenumber range of interest and the vector $\mathbf{v}(\omega)$ represents wavenumber values of the continuous frequency-wavenumber spectrum $V(\kappa, \omega)$. Only a small number M of modes, i.e., wavenumbers, is excited in a given experiment. Hence, $\mathbf{v}(\omega)$ is very sparse. We rewrite the signal model (2) in matrix-vector form as

$$\mathbf{x}(\omega) = \Phi \mathbf{v}(\omega) + \mathbf{w}(\omega), \tag{6}$$

where the (l, n)th entry of the $L \times N$ matrix Φ is given by

$$[\Phi]_{ln} = \frac{1}{\sqrt{\kappa_n r_l}} e^{j r_l \kappa_n}, \tag{7}$$

and the noise vector is given by

$$\mathbf{w}(\omega) = [W(r_1, \omega) \;\; W(r_2, \omega) \cdots W(r_L, \omega)]^T. \tag{8}$$

The next subsection uses the model in Eq. (6) to formulate CCSWA and solves for the sparse vector $\mathbf{v}(\omega)$ using a continuity constraint.

B. Continuity constrained sparse reconstruction

As noted above, the vector $\mathbf{v}(\omega)$ is highly sparse since it contains only M ($\ll N$) non-zero elements specified by the nonzero terms $G_m(\omega)$ at $\kappa = k_m(\omega)$. Hence, we can formulate the dispersion curve reconstruction problem as a sparse optimization problem[34–37]

$$\begin{aligned} &\mathbf{v}(\omega) = \underset{\mathbf{v}(\omega)}{\operatorname{argmin}} \|\mathbf{v}(\omega)\|_0, \\ &\text{subject to } \; ||\mathbf{x}(\omega) - \Phi \mathbf{v}(\omega)||_2 \le \delta, \end{aligned} \tag{9}$$

where $||\mathbf{v}(\omega)||_0$ is the l_0-pseudo-norm defined as the number of non-zero elements in $\mathbf{v}(\omega)$, and $||\cdot||_2$ is the l_2 norm. Differing from prior work,[8] we introduce δ as a bound on the reconstruction error ϵ,

$$||\mathbf{x}(\omega) - \mathbf{x}_0(\omega)||_2 = \epsilon \le \delta, \tag{10}$$

where $\mathbf{x}_0(\omega)$ is an ideal noiseless signal. We remark later that this bound leads to an effective solution of Eq. (9) in the presence of noise. We turn problem (9) into the *LASSO* regression problem,[38–40] or, equivalently, basis pursuit (BP), by relaxing the l_0-pseudo-norm in Eq. (9) to the l_1-norm

$$\tilde{\mathbf{v}}(\omega) = \underset{\tilde{\mathbf{v}}(\omega)}{\operatorname{argmin}} \|\Phi \tilde{\mathbf{v}}(\omega) - \tilde{\mathbf{x}}(\omega)\|_2^2 + \tau \|\boldsymbol{\eta}(\omega) \odot \tilde{\mathbf{v}}(\omega)\|_1, \tag{11}$$

where τ is the regularization parameter, $\|\cdot\|_1$ denotes the l_1 norm, and $\odot$ denotes elementwise multiplication. The vector $\tilde{\mathbf{x}}(\omega) = \mathbf{x}(\omega)/||\mathbf{x}(\omega)||_2$ is normalized. Note that a frequency dependent weight factor $\boldsymbol{\eta}(\omega) = [\eta(\omega)_1, \eta(\omega)_2, \ldots, \eta(\omega)_N]^T$ is introduced in the l_1 regularization term in Eq. (11) to enforce continuous reconstruction, which makes Eq. (11) different from the classic LASSO formulation. The first term in Eq. (11) attempts to ensure model fitting, while the second term in Eq. (11) imposes sparsity on the solution. Therefore, when values of $\boldsymbol{\eta}$ are large, we impose more strongly sparsity at the corresponding wavenumber. When values of $\boldsymbol{\eta}$ are small, we impose more strongly model fitness at the corresponding wavenumber. When $\boldsymbol{\eta} = 1$, Eq. (11) reduces to the classic SWA formulation.[8]

We next consider that we probe the structure with Q frequencies. When we stack together all of the solutions to Eq. (11) for the Q frequencies of interest, we get the matrix formulation

$$\tilde{\mathbf{V}} = \underset{\tilde{\mathbf{V}}}{\operatorname{argmin}} \|\Phi \tilde{\mathbf{V}} - \tilde{\mathbf{X}}\|_2^2 + \tau \|\Theta \odot \tilde{\mathbf{V}}\|_1, \tag{12}$$

where $\tilde{\mathbf{X}} = [\tilde{\mathbf{x}}_1, \tilde{\mathbf{x}}_2, \ldots, \tilde{\mathbf{x}}_Q]$, $\tilde{\mathbf{V}} = [\tilde{\mathbf{v}}_1, \tilde{\mathbf{v}}_2, \ldots, \tilde{\mathbf{v}}_Q]$, and $\Theta = [\boldsymbol{\eta}_1, \boldsymbol{\eta}_2, \ldots, \boldsymbol{\eta}_Q]$, respectively. Each column of these

matrices corresponds to one of the Q frequencies. The goal of this optimization formulation is to extract the dispersion curve matrix $\tilde{\mathbf{V}}$ across all frequencies and wavenumbers of interest.

1. Remark

Given the sensing matrix Φ and assuming the noise is absent, basis pursuit provides an accurate reconstruction of $\mathbf{v}_0(\omega)$ from the noiseless data $\mathbf{x}_0(\omega)$ if the restricted isometry property (RIP) is satisfied.[41] Reference 42 proves that RIP is satisfied with random sensor topologies. In the noisy case,[43] if the noise is bounded $||\mathbf{x}(\omega) - \mathbf{x}_0(\omega)||_2 \leq \delta$, and $\mathbf{v}_0(\omega)$ satisfies the sparse requirement

$$||\mathbf{v}_0(\omega)||_0 < \frac{1}{4}\left(1 + \frac{1}{\gamma}\right), \tag{13}$$

where γ denotes the mutual coherence of Φ,[43] then the reconstruction is stable, and the reconstruction error $||\tilde{\mathbf{v}}(\omega) - \mathbf{v}_0(\omega)||_2$ is, at worst, proportional to the noise level bound δ. For Eq. (11), the requirement in Eq. (13) is satisfied since γ is close to zero. If we properly choose the regularization parameter τ in Eq. (11) to be between 0 and $||\Phi^H \mathbf{x}(\omega)||_\infty$, then the solution $\tilde{\mathbf{v}}(\omega)$ to the sparse reconstruction problem (11) shares the same support as the unique optimal solution $\mathbf{v}_0(\omega)$ for which noise is absent.[36] Therefore, we can solve the sparse reconstruction problem in Eq. (9) by finding the solution to Eq. (11) in the presence of noise.

2. Signal synthesis

As in prior work,[8] once we obtain the reconstructed $\tilde{\mathbf{v}}(\omega)$, we can predict the signal $\hat{\mathbf{x}}(\omega)$ at chosen distances $\mathbf{r}^* = [r_1^*, r_2^*, \ldots, r_L^*]$ from the transmitter by solving the following forward problem:

$$\hat{\mathbf{x}}(\omega) = \hat{\Phi}\tilde{\mathbf{v}}(\omega), \tag{14}$$

where the (l, n)th entry of the $L \times N$ matrix $\hat{\Phi}$ corresponds to the distance r_l^* such that

$$[\hat{\Phi}]_{ln} = \frac{1}{\sqrt{\kappa_n r_l^*}} e^{jr_l^* \kappa_n}.$$

This is referred to as sparse wavenumber synthesis (SWS).[8] If in Eq. (14), we take the distance $r_l^* = r_l$ for all $l = 1, \ldots, L$ (i.e., at the sensor locations), then Eq. (14) synthesizes the signal at each of the L sensors from the reconstructed $\tilde{\mathbf{v}}(\omega)$. This is referred to as sparse wavenumber denoising (SWD)[8] and re-synthesizes the measured signals from the sparse representation with significant noise reduction. We refer to these signals as denoised signals.[8] These signals can then be used by other methods like matched field processing in defect localization, see Sec. III.

C. Description of the CCSWA algorithm

In this subsection, we describe the CCSWA algorithm to reconstruct dispersion curves. The six steps of the CCSWA algorithm are as follows: (1) perform original SWA, (2) detect outliers by edge detection, (3) increase weights for outliers, (4) remove outliers by CCSWA, (5) identify each wave mode by clustering and adjust the weights $\boldsymbol{\eta}(\omega)$ by polynomial fitting, (6) restore missing points by CCSWA. The specific steps of the CCSWA algorithm are provided as follows.

Step 1: Obtain $\tilde{\mathbf{V}}$ by unweighted SWA. In this step, the original basis pursuit problem is solved by the original SWA method[8] to obtain $\tilde{\mathbf{V}}$. Note that the $\tilde{\mathbf{V}}$ is obtained without imposing the continuity constraint.

Step 2: Detect outliers. In this step, we treat the reconstructed dispersion curves $\tilde{\mathbf{V}}$ from step 1 as an image with each point in $\tilde{\mathbf{V}}$ as a pixel in the image. The dispersion curves are considered as edges in the image, and the edges are to be detected by the directional gradient of the pixel intensity. The points falling on these edges define set U, and the points not in this set, $\bar{U} = \{x : x \notin U\}$, are outliers. We approximate the gradient at each pixel in the image by a differential operator, the Sobel operator (commonly used in image processing[44]). Applying the Sobel operator, all points with gradients larger than a threshold are treated as edges. We refer to this threshold as the Sobel threshold s and define it in Sec. III. Figure 1 illustrates that the pixels in the dispersion curves change intensity in the direction normal to the curves, and can thus be detected as edges.

Step 3: Increase the penalty for outliers. In this step, we increase the weight $\eta_{\kappa_i}^{\bar{U}}(\omega)$ in Eq. (11) to a value greater than 1 for each outlier identified in $\bar{U}$. We describe how we choose the weight increase in Sec. III. This promotes further sparsity at the locations of these points. Hence, we penalize the reconstruction of points that are far from the dispersion curves.

Step 4: Remove outliers by CCSWA. In this step, CCSWA is performed with the increased weights $\boldsymbol{\eta}(\omega)$ that penalize outliers. This results in a noise-reduced $\tilde{\mathbf{V}}$. The points in $\tilde{\mathbf{V}}$ define set O. We use $\eta_{\kappa_i}^{O}(\omega)$ to denote the associated weight

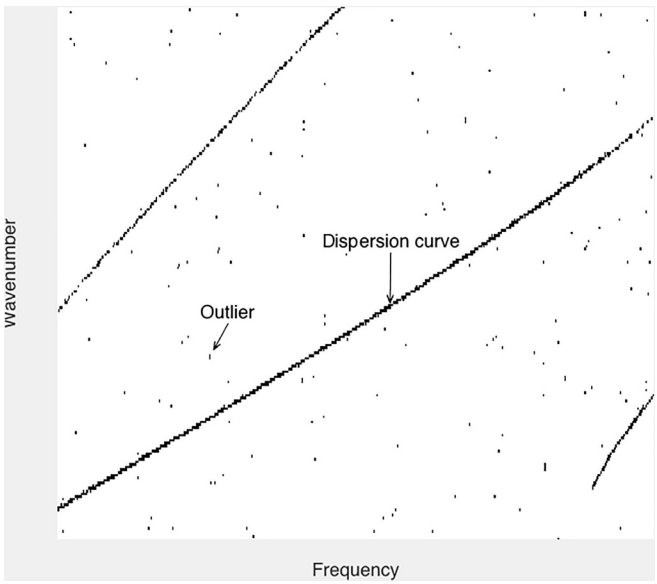

FIG. 1. Pixels in dispersion curves. The pixels in the dispersion curves with changing intensity in the direction normal to the curves are detected as edges. The remaining pixels are outliers.

for point in O at frequency ω and at wavenumber κ_i. We describe how we choose the weight in Sec. III. After this step, a much smaller number of outliers will remain in the dispersion curves. However, while outliers are removed, some points in the recovered dispersion curves may also be removed. This is because isolated points on the dispersion curves are treated as outliers. In the following steps, we restore these missing points.

Step 5: Adjust weights $\boldsymbol{\eta}(\omega)$ by clustering. In this step, we implement variational Bayes Gaussian mixture model clustering to identify the modes on the dispersion curves. This is a common probability density based clustering algorithm that uses a Bayesian framework and a variational method to approximate the *posterior* distribution of the latent variables, i.e., the mean, the variance, and the model mixing coefficient, in a finite mixture of Gaussian components, as well as to estimate the number of components.[45–48] The points in O are clustered into T clusters. To predict the positions of the missing points, we fit the obtained T clusters with T quadratic polynomials $\{h_t(x) : x \in O, t = 1, \ldots, T\}$, each $h_t(x)$ being a quadratic polynomial fitted on the positions of points in the tth cluster. Since predicted positions are not precisely on the dispersion curves, we define a region $\Omega \supseteq O$, $\Omega = \{y : h(x) - \Delta \leq y \leq h(x) + \Delta, x \in O\}$, where Δ is the distance between the position of each point y in this region and the polynomial spline $h(x)$. The weights $\eta^{\Omega}_{\kappa_i}(\omega)$ for positions in this region Ω are then decreased to promote greater model fitness. We describe how we choose the weight decrease in Sec. III.

Step 6: Restore missing positions by CCSWA. In this step, CCSWA is repeated with the decreased weights $\boldsymbol{\eta}(\omega)$ from step 5. This procedure restores the missing points in the dispersion curves that were incorrectly removed by edge detection in step 4. The dispersion curves become much smoother, continuous in frequency, and the noise is removed.

The sparse reconstruction algorithm is summarized in Algorithm 1.

Algorithm 1: CCSWA

Input: Measurement matrix $\tilde{\mathbf{X}} = [\tilde{\mathbf{x}}_1, \tilde{\mathbf{x}}_2, \ldots, \tilde{\mathbf{x}}_Q]$, sensing matrix Φ
Output: Frequency-wavenumber representation $\tilde{\mathbf{V}} = [\tilde{\mathbf{v}}_1, \tilde{\mathbf{v}}_2, \ldots, \tilde{\mathbf{v}}_Q]$
begin
(1) **Initialize** weight: $\Theta = [\boldsymbol{\eta}_1, \boldsymbol{\eta}_2, \ldots, \boldsymbol{\eta}_Q] \leftarrow \mathbf{I}$
(2) **for** $i \leftarrow 1$ **to** Q **do**
  $\tilde{\mathbf{v}}_i \leftarrow$ unweighted SWA$(\tilde{\mathbf{x}}_i, \Phi)$
(3) **Detect outliers** $\bar{U}$ **in** $\tilde{\mathbf{V}}$
(4) **foreach** $\eta^{\bar{U}}_{\kappa_i}(\omega) \in \Theta$ **do**
  Update $\eta^{\bar{U}}_{\kappa_i}(\omega) \leftarrow \eta^{\bar{U}}_{\kappa_i}(\omega) > 1$
(5) **for** $i \leftarrow 1$ **to** Q **do**
  $\tilde{\mathbf{v}}_i \leftarrow \text{CCSWA}(\tilde{\mathbf{x}}_i, \Phi, \boldsymbol{\eta}_i)$
  $O = O \cup \{\mathbf{v}_i\}$
(6) **Cluster** $\tilde{\mathbf{V}}$ **and polynomially fit clusters to** Ω
(7) **for each** $\eta^{\Omega}_{\kappa_i}(\omega) \in \Theta$ **do**
  Update $\eta^{\Omega}_{\kappa_i}(\omega) \leftarrow \eta^{\Omega}_{\kappa_i}(\omega) < 1$
  $\eta^{O}_{\kappa_i}(\omega) \leftarrow \eta^{O}_{\kappa_i}(\omega) < \eta^{\Omega}_{\kappa_i}(\omega)$
(8) **for** $i \leftarrow 1$ **to** Q **do**
  $\tilde{\mathbf{v}}_i \leftarrow \text{CCSWA}(\tilde{\mathbf{x}}_i, \Phi, \boldsymbol{\eta}_i)$
return $\tilde{\mathbf{V}}$

III. NUMERICAL SIMULATIONS AND EXPERIMENTS

In this section, we apply CCSWA to numerical simulated data and to laboratory experimental data. We present the results and analyze the performance of the CCSWA procedure.

A. Simulation and experimental setup

To compare the performance of different dispersion curves reconstruction algorithms, we process the simulation and experimental settings and data used in previous work.[8] We briefly detail these here. We consider a 0.284 cm thick, 1.22 m long, and 1.22 m wide aluminum plate, with a collection of 17 randomly placed PZT transducers on the surface of the plate. We refer to prior work[8] for exact sensor positions. The random sensor topology helps to improve localization performance in matched field processing.[49] The lead zirconate titanate transducer in use has resonant frequency of 240 kHz, and resonant impedance smaller than 18 Ω. This is well-suited for our study. The transmitted signal is a 10 μs linear frequency modulated chirp with a 3 dB bandwidth between 0 and 2 MHz. In both simulations and experiments, we compute the sparse representations over the same discretized frequency range from 0 to 1 MHz.

In the simulations, we generate the signal according to Eq. (1) with complex amplitudes for each mode set to $G_m(\omega) = 1$. The process is repeated 17 times, where in each iteration we choose one of the transducers on the plate to transmit a chirp signal that is then received by each of the other 16 transducers. The multipath effects are simulated by ray tracing additional paths reflected by the rigid boundaries of the plate. The signals are windowed using a rectangular window with an exponential taper to remove late arrivals.

In the experiments, for every pair of transmitter-transducer and receiver-transducer, we collect the received data, which provides a total of 272 different measurements for 136 unique distances. The initial 10 μs of each measurement is windowed out to remove cross-talk. When testing localization, we use matched field processing to locate two 0.75 cm holes near the center of the plate and separated by a 6.5 cm distance. We assume the hole is represented by a point reflector that re-transmits the incident wave equally in all directions. This is a standard target model assumed by many localization algorithms and remains a valid approximation as long as the size of the hole is sufficiently smaller than the wavelength. For larger targets or very small wavelengths, we may need to model the hole as an extended target. In this paper, we show that, even with the simplistic omni-directional model we assume, the localization results we obtain are very good.

Our goal with the simulations and experiments is to compare the performance of our method with the classic SWA[8] method with respect to (1) reconstructing the dispersion curves, (2) predicting signals at arbitrary sensor locations, (3) evaluating the correlation coefficients between the true signals and the synthesized signals, (4) evaluating the effect of reducing the number of sensors, and (5) localizing holes on the plate. We use the correlation coefficient c between the true signal and the signal synthesized by sparse

wavenumber synthesis (see Sec. II B) as the metric that measures the effectiveness of CCSWA under a set of parameter configurations. Given an arbitrary distance $\hat{r}$ between the transmitter and a receiver, we can predict the signal response $\hat{\mathbf{x}}$ at the receiver at each frequency ω using the sparse wavenumber synthesis given by Eq. (14). The correlation coefficient between the measured signal $\mathbf{x}$ and the predicted signal $\hat{\mathbf{x}}$ is defined as[8]

$$c = \frac{\sum_{q=1}^{Q} \mathbf{x}(\omega_q)^H \hat{\mathbf{x}}(\omega_q)}{\sqrt{\sum_{q=1}^{Q} ||\mathbf{x}(\omega_q)||_2^2} \sqrt{\sum_{q=1}^{Q} ||\hat{\mathbf{x}}(\omega_q)||_2^2}}, \tag{15}$$

where Q is the number of frequencies of interest, and $\mathbf{x}(\omega_q)$ is the signal response at the qth frequency.

B. Parameter tuning

The CCSWA algorithm contains parameters, specifically, the Sobel threshold s, the number of clusters t, the weight vector $\boldsymbol{\eta}$, and the regularization parameter τ. These parameters must be tuned in order to achieve optimal performance. We now show tuning of the parameters in the CCSWA algorithm.

1. Threshold for Sobel edge detection

Figure 2 illustrates the outliers detected by the Sobel operator. We observe a significant number of small spikes between the ridges. These spikes represent "noise" in the reconstructed frequency-wavenumber domain, which are the result of the simulated reflection and multipath interference in the simulation data. In the experimental data, there is additional uncertainty caused by transducers, the medium, and the testing environment. Table I shows the average correlation coefficients between true and synthesized signals with respect to different Sobel thresholds s over 200 samples. In the table, the denoised signal represents the signal without multipath interference and noise, and the predicted signal represents the signal response at the receiver for an arbitrary transmitter and receiver pair. We find that a reasonable choice for the Sobel threshold s is in the range $(0.01, 0.02)$.

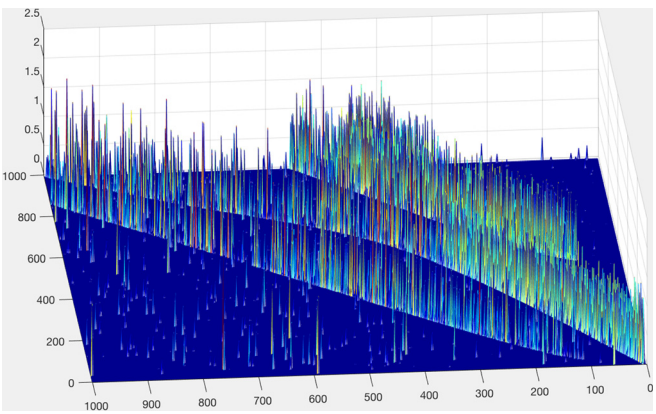

FIG. 2. (Color online) Outliers detected by the Sobel operator.

2. Number of clusters t

In variational Bayes Gaussian mixture model[45–48] clustering, we start with an initial estimate of the number of candidate Gaussian components. The algorithm eventually determines the optimal number of Gaussian components, i.e., the number of clusters. Figure 3 illustrates the clustering and polynomial fitting results for different choices of the initial number of candidate Gaussian components. We see that, for an initial guess smaller than 5, the algorithm is not able to distinguish different modes. For larger initial guesses, e.g., 10, different modes are successfully clustered into the correct clustering groups. We note that for the $S0$ mode four Gaussian components are chosen to model the distribution of the points on the mode. By setting a large initial guess, we remove outliers by thresholding the size of the clusters. As the initial guess grows larger, the clustering results remain unchanged. We choose the initial number of Gaussian components to be 15, which clusters the dispersion curves into $t = 7$ groups, i.e., a mixture of seven Gaussian components is used to model the data distribution. The solid lines in Fig. 3 illustrate the polynomial splines fitting the points in the clusters. Figure 3 shows that these lines predict the positions of the $[k_i(\omega), \omega]$ pairs that belong to the continuous modes. Intuitively, we reduce the cost in Eq. (11) for reconstructing these positions by decreasing the value of their weights to $\eta_{\kappa_i}(\omega) < 1$, thus encouraging reconstruction of these points.

3. Weight $\boldsymbol{\eta}(\omega)$

The choice of weight $\boldsymbol{\eta}(\omega)$ in Eq. (11) is crucial to balance the sparsity requirement and the frequency continuity requirement and can significantly affect the sparse reconstruction results. We apply three different weights, $\eta_{\kappa_i}^{\bar{U}}$, $\eta_{\kappa_i}^{O}$, and $\eta_{\kappa_i}^{\Omega}$, as shown in Fig. 4 and described in Sec. II C. We use $\eta_{\kappa_i}^{\bar{U}}$ to weight the outliers detected by edge detection, $\eta_{\kappa_i}^{O}$ to weight the points reconstructed by CCSWA, and $\eta_{\kappa_i}^{\Omega}$ to weight the points predicted by clustering and polynomial fitting. As a result of these weights, the points at different wavenumbers in the dispersion curves $\tilde{\mathbf{v}}(\omega)$ will have different reconstruction costs. Larger values of $\eta_{\kappa_i}(\omega)$ promote sparsity, while smaller values promote model fitting. In **step 3** of the algorithm, we set the weights of $\eta_{\kappa_i}^{\bar{U}}(\omega)$ in the range $(1.5, 4.0)$, while the remaining weights $\eta_{\kappa_i}^{U}(\omega)$ equal 1. In

TABLE I. Average correlation coefficients for different Sobel thresholds. Average correlation coefficients over 200 samples between true and synthesized signals using different Sobel thresholds.

	Correlation coefficient	
Sobel threshold	True and denoised signal	True and predicted signal
0.01	0.7590	0.7631
0.02	0.7306	0.7295
0.03	0.6984	0.6974
0.05	0.6685	0.6635

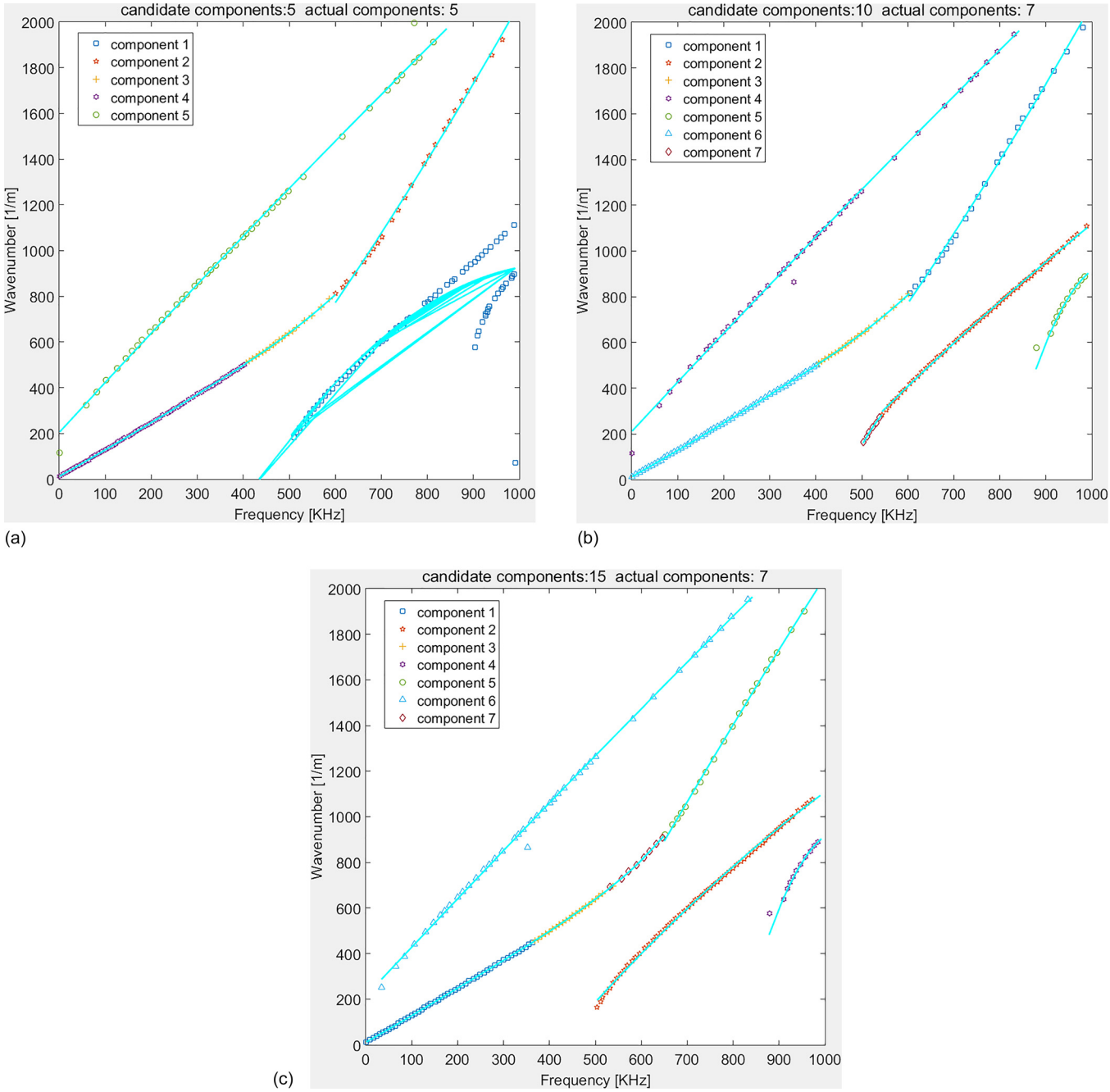

FIG. 3. (Color online) Clustering and polynomial fitting results for different choices of the initial number of candidate Gaussian components: (a) initial number of candidate Gaussian components: 5, actual number of Gaussian components: 5; (b) initial number of candidate Gaussian components: 10, actual number of Gaussian components: 7; (c) initial number of Gaussian components: 15, actual number of Gaussian components: 7. The solid lines represent the polynomials that fit the data.

step 5 of the algorithm, we set the weights of $\eta^{O}_{\kappa_i}(\omega)$ in the range $(0.5, 0.95)$, and we set the weights of $\eta^{\Omega}_{\kappa_i}(\omega)$ in the range $(0.25, 0.9)$. We enforce $\eta^{\Omega}_{\kappa_i}(\omega) > \eta^{O}_{\kappa_i}(\omega)$ in order to tolerate some prediction errors. For positions outside O, we set the weights $\eta^{\bar{O}}_{\kappa_i}(\omega)$ in the range $(1.5, 4.0)$. We choose $\Delta = 10$ to define the region Ω. Figure 5 shows an overview of the weighting protocol.

4. Regularization parameter τ

The regularization parameter τ in Eq. (11) describes how much the overall reconstruction process stresses sparsity. A large τ promotes a sparser $\mathbf{v}$ and avoids overfitting the linear model. We set τ in the range $(0.45, 0.5)$, the same as in prior work.[8] There are also methods that automatically selects the proper value for τ, such as the in-crowd algorithm[50] and the homotopy continuation-based algorithm.[51]

C. Simulation results and discussion

In this subsection, we compare the simulation results obtained with CCSWA with the results obtained with the original SWA. We consider two versions of SWA: (1) sparse

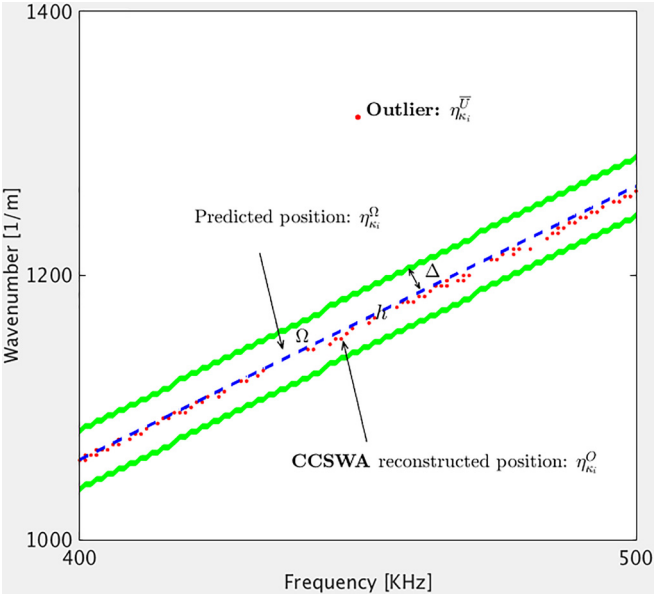

FIG. 4. (Color online) Illustration of three different weights, $\eta^{\bar{U}}_{\kappa_i}$, $\eta^{O}_{\kappa_i}$, and $\eta^{\Omega}_{\kappa_i}$. The dashed line denotes the polynomial h that predicts the positions of dispersion curves. The region Ω is defined within distance Δ from the polynomial h.

wavenumber analysis using basis pursuit[8] (BPSWA) and (2) orthogonal matching pursuit (OMP).[10,30–32] The comparison is based on the quality of the reconstructed dispersion curves and the synthesized signals.

1. Reconstruction of dispersion curves

Figure 6 illustrates the dispersion curves for Lamb waves reconstructed using BPSWA, OMP, and CCSWA, respectively, with 1000 frequencies uniformly sampled from 0 to 1 MHz. The dispersion curves illustrated in Fig. 6 show that all three methods—BPSWA, OMP, and CCSWA—have

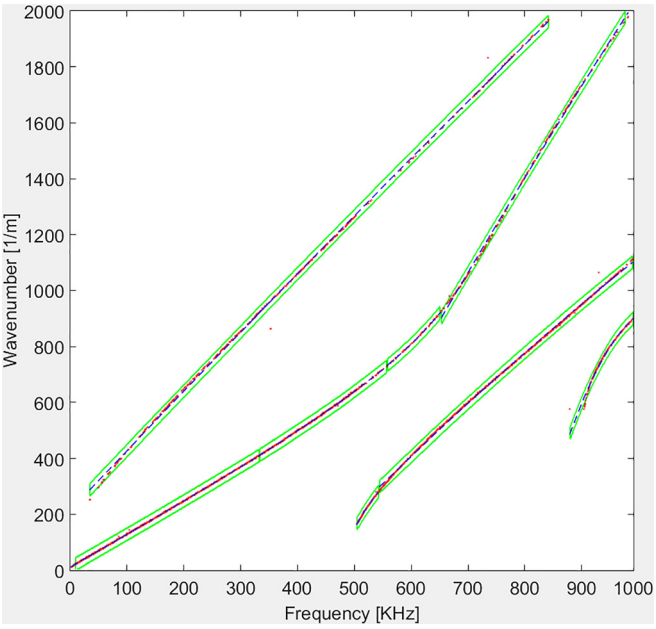

FIG. 5. (Color online) Overview of the weighting protocol. The dotted line denotes positions reconstructed by CCSWA. The dashed line denotes positions predicted by polynomial.

reconstructed the four modes of the dispersion curves, namely, $A0$, $S0$, $A1$, $S1$, across a 1 MHz bandwidth successfully. However, the dispersion curves in Fig. 6(a) by BPSWA and Fig. 6(b) by OMP are noisier and show several discontinuities in frequency. For the $A0$ mode, the BPSWA and OMP curves have broken line segments at frequencies lower than 150 kHz and at frequencies between 500 and 800 kHz. For the $S0$ mode, the curves show occasional line segments in frequencies higher than 500 kHz. These are reconstruction errors induced by reflection and multipath interference in the data samples. This confirms that the reconstructed dispersion curves with SWA (Ref. 8) are fragmented, even though they should be continuous. CCSWA overcomes this limitation, as shown in Fig. 6(c). CCSWA shows recognizably good performance for all four modes. The dispersion curves are smooth, continuous, and free of noise.

2. Signal synthesis

Figure 7(a) illustrates a denoised signal at a receiver location 0.89 m from the transmitter, as synthesized by continuity constrained SWD (CCSWD), SWD by basis pursuit[8] (BPSWD), and SWD by OMP (OMPD),[10,30–32] respectively. Figure 7(a) shows that all three methods remove the multipath interference from the measured signal. Yet, the CCSWD result best resembles the true signal, especially in the time interval $0.25 - 0.3$ ms. Figure 7(b) illustrates a predicted signal computed with Eq. (14) at a receiver location 0.58 m from the transmitter, as synthesized by continuity constrained SWS (CCSWS), SWS using basis pursuit[8] (BPSWS), and SWS using OMP (OMPS),[10,30–32] respectively. Figure 7(b) shows that all three methods predict the true signal. Yet, the CCSWS result best resembles the true signal, especially in the time interval $0.16 - 0.2$ ms.

Figure 8(a) illustrates the correlation coefficients between the true signals and denoised signals with CCSWS, BPSWS, and OMPS, respectively. The average correlation coefficients using BPSWD and OMPD are 0.85 and 0.80 (Table II), respectively. In contrast, the average correlation coefficient using CCSWD is 0.89. Note that the correlation coefficients for some measurements (measurement 0, 20, 30, 40, 60) decrease abruptly because they correspond to sensor locations at the boundary of the plate, where the interference significantly reduces the signal-to-noise ratio. Figure 8(b) shows that the average correlation coefficients between the true signals and the predicted signals using BPSWS and OMPS are 0.86 and 0.79 (Table II). In contrast, the correlation coefficient using CCSWS increases to 0.90.

D. Experimental results and discussion

In this subsection, we compare the experimental results from CCSWA with the original SWA, implemented again with two algorithms: (1) sparse wavenumber analysis using BPSWA,[8] and (2) OMP.[10,30–32] The comparison is made based on the reconstructed dispersion curves and the synthesized signals with a reduced number of measurements. Matched field processing is carried out at the end to verify the effectiveness of CCSWA for localizing damage.

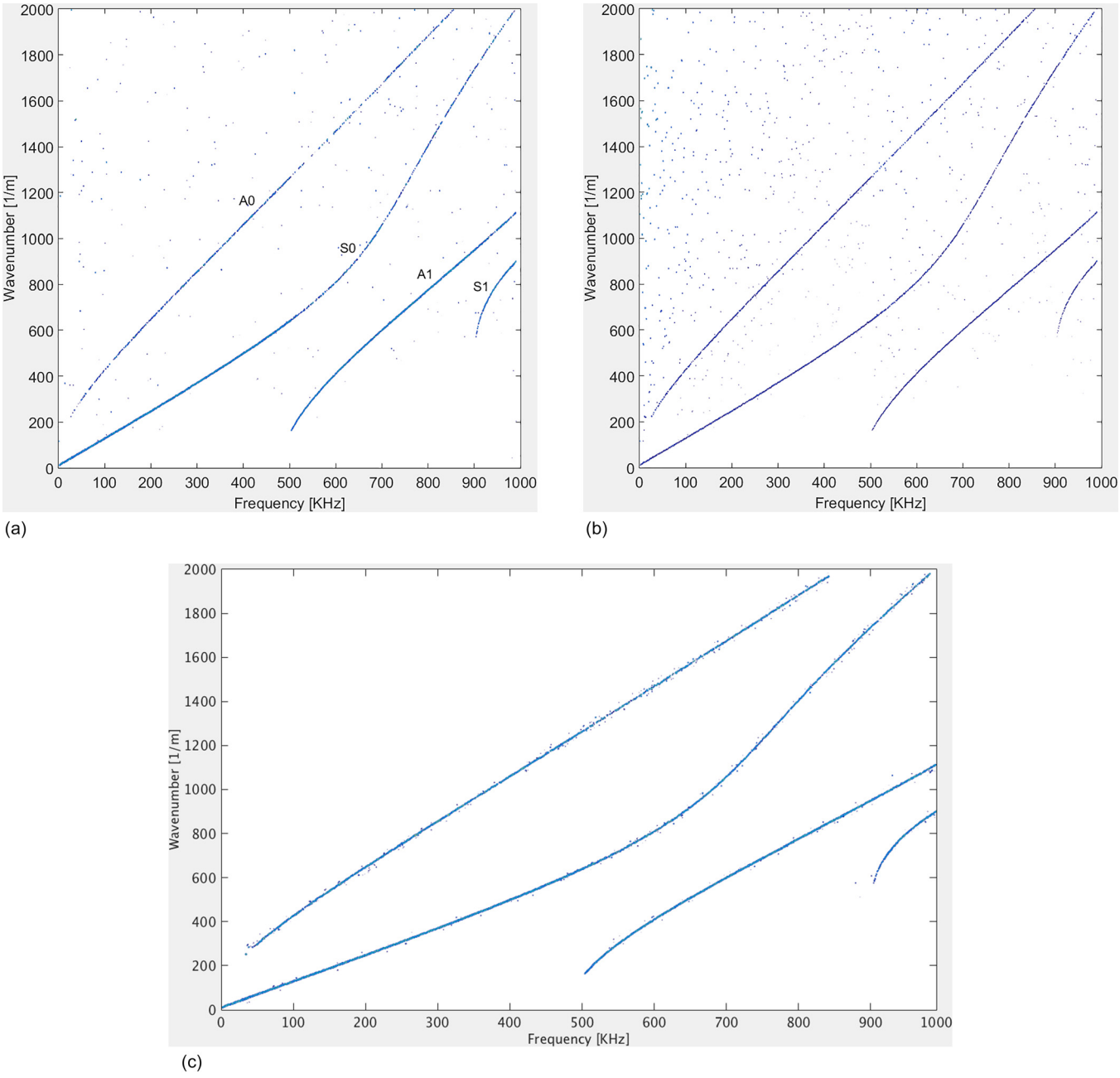

FIG. 6. (Color online) Dispersion curves reconstructed by (a) BPSWA, (b) OMP, and (c) CCSWA using simulation data with 1 MHz bandwidth.

1. Reconstruction of dispersion curves

Figure 9 illustrates the dispersion curves for Lamb waves reconstructed using BPSWA, OMP, and CCSWA, respectively, with 1000 frequencies uniformly sampled from 0 to 1 MHz. The BPSWA dispersion curves in Fig. 9(a) are corrupted with noise at frequencies higher than 800 kHz. The OMP dispersion curves in Fig. 9(b) exhibit significant noise overall. Both BPSWA and OMP $A0$, $S0$, $A1$ modes consist of several line fragments. In contrast, we see in Fig. 9(c) that the three modes are well reconstructed by CCSWA. The curves are noise free and are continuous with respect to frequency. The modes $A0$, $S0$, and $A1$ disappear for wavenumbers between 700 and 900 m^{-1}. This is because this range corresponds to wavelengths between 0.7 and 0.9 cm that are on the order of the transducer dimensions, which causes scattering and attenuation at those wavelengths.[52] The $S1$ mode vanishes around 900 kHz due to a small group velocity and small magnitude. Better reconstruction results could be achieved if we had used smaller transducers and stronger signal strength.

2. Signal synthesis with reduced measurements

In this subsection, we analyze the accuracy of signal synthesis with reduced numbers of measurements. Table III shows the average correlation coefficients between the true signals and the denoised signals with different numbers of transducers. Table III reveals that the signal synthesis

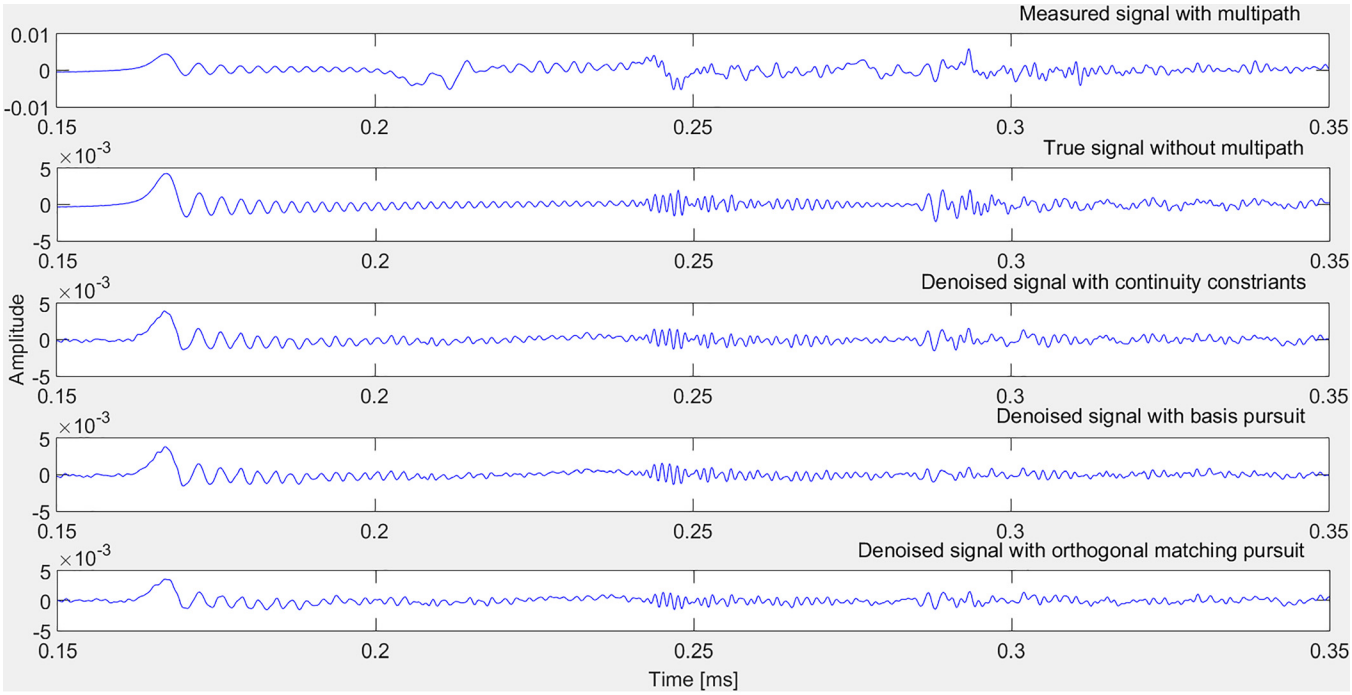

(a)

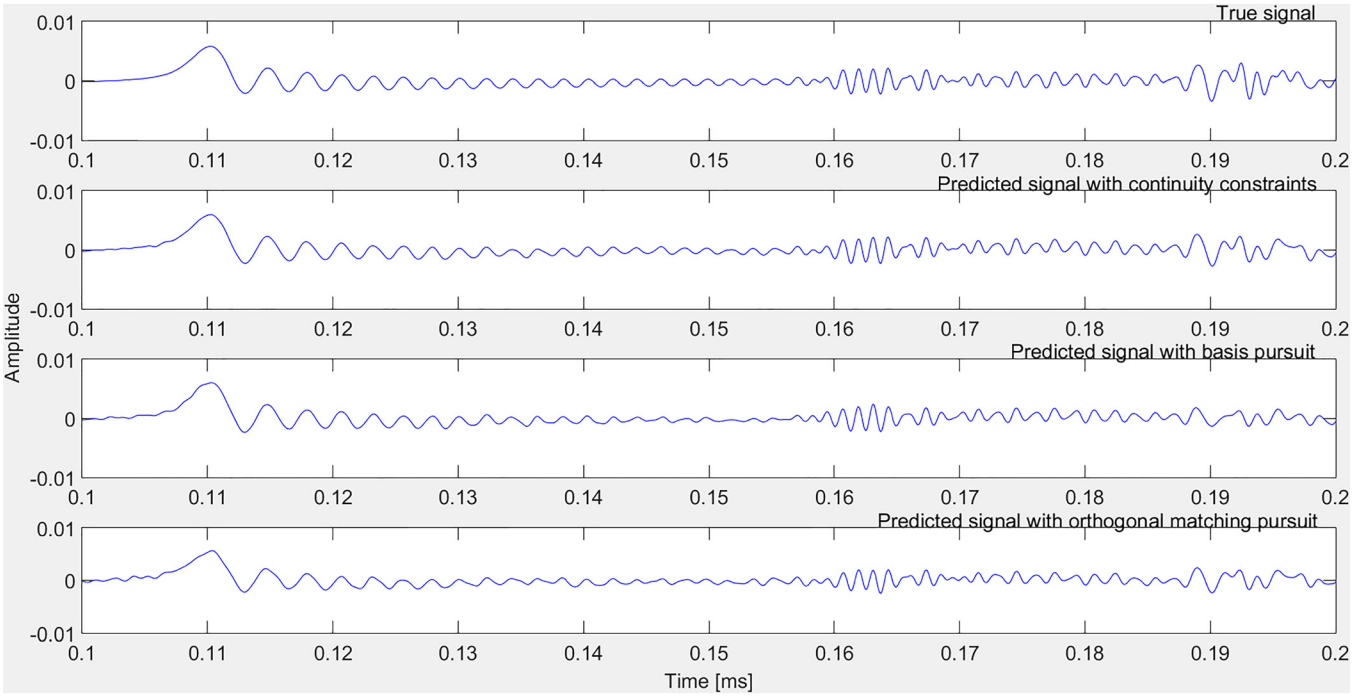

(b)

FIG. 7. (Color online) (a) Signal responses at the receiver 0.89 m from the transmitter generated with simulation data. Each row corresponds to the measured signal with multipath interference, the true signal without multipath interference, the signal denoised by CCSWD, the signal denoised by BPSWD, and the signal denoised by OMPD, respectively. (b) Signal responses at an arbitrary receiver 0.58 m from the transmitter generated with simulation data. Each row corresponds to the true signal, the predicted signal by CCSWS, the predicted signal by BPSWS, and the predicted signal by OMPS, respectively.

accuracy with BPSWD deteriorates dramatically when the number of measurements is decreased by approximately 80% (from 272 measurements with 17 sensors to 56 measurements with 8 sensors). The accuracy of OMPD also decreases significantly. This is expected because the restricted isometry property required for sparse reconstruction is no longer valid. The continuity constrained CCSWD achieves much greater robustness to measurement numbers.

3. CCSWA + matched field processing

We integrate CCSWA with matched field processing to locate damage. Matched field processing (MFP) utilizes

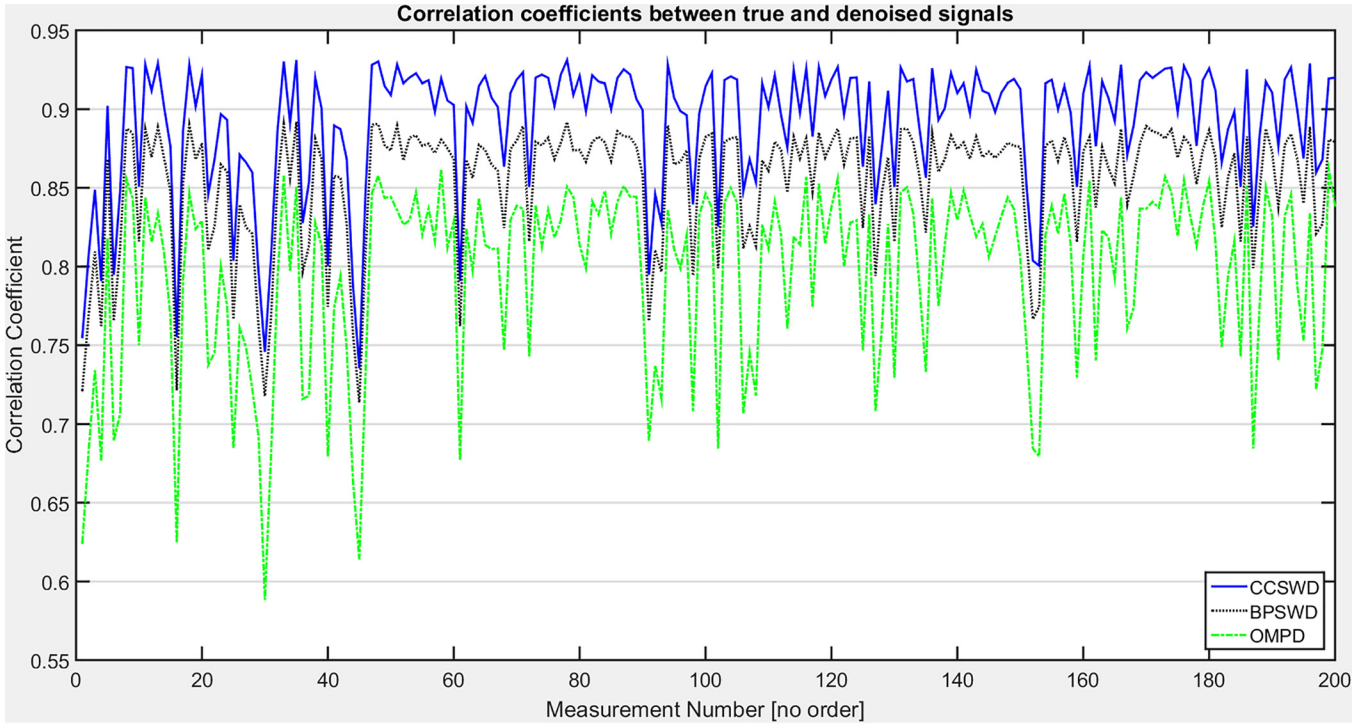

(a)

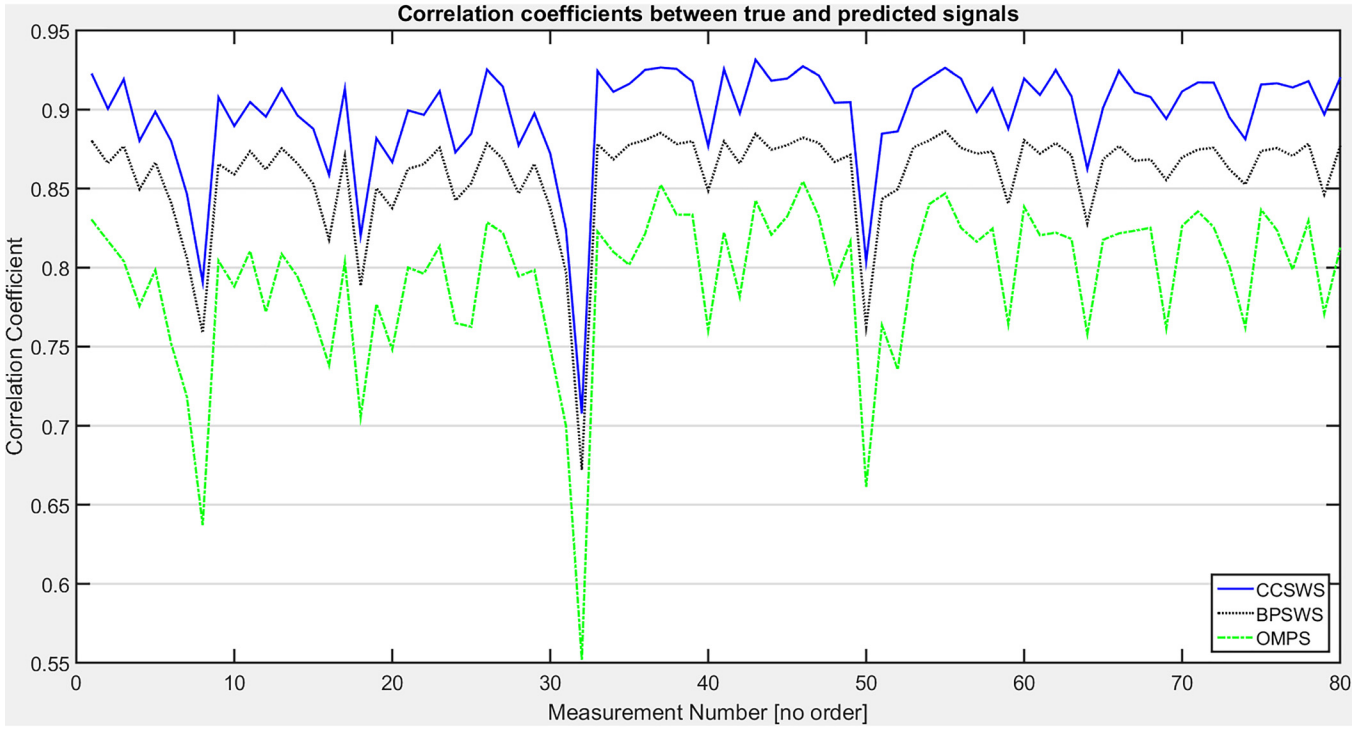

(b)

FIG. 8. (Color online) (a) Correlation coefficients between 200 measured true signals and their corresponding denoised signals using CCSWD, BPSWD, and OMPD with simulation data. (b) Correlation coefficients between 80 measured true signals and their corresponding predicted signals using CCSWS, BPSWS, and OMPS with simulation data.

wavefield propagation modeling to find the location of an acoustic source.[53–55] MFP has been extensively used in underwater acoustics, seismology, and nondestructive testing.[28,56] Instead of using the wave propagation equation, we build the propagation model with sparse wavenumber synthesis. The output of the matched field processor is the ambiguity function $b(\mathbf{r})$,[28] which is the squared magnitude of the correlation between the measured signal $\mathbf{x}(\omega_q)$ and the synthesized signal $\hat{\mathbf{x}}(\omega_q)$ across the frequencies $[\omega_1, \omega_2, \ldots, \omega_Q]$,

TABLE II. Average correlation coefficients for different signal synthesis methods. The average correlation coefficients between true and synthesized signals from simulation with CCSWS, BPSWS, and OMPS, respectively.

	True and denoised signal	True and predicted signal
CCSWS	0.89	0.90
BPSWS	0.85	0.86
OMPS	0.80	0.79

$$b(\mathbf{r}) = \frac{\left|\sum_{q=1}^{Q} \mathbf{x}(\omega_q)^H \hat{\mathbf{x}}(\omega_q)\right|^2}{\sum_{q=1}^{Q} ||\hat{\mathbf{x}}(\omega_q)||_2^2}. \quad (16)$$

TABLE III. Average correlation coefficients between true and denoised signals synthesized from experimental data with different number of sensors.

No. of sensors	CCSWD	BPSWD	OMPD
17	0.92	0.84	0.84
8	0.87	0.59	0.79

The ambiguity function measures the "fitness" between the measured data and the model. From Eq. (16), we see that the resolution of the output of the matched field processor depends on the correlation between the measured signal and the predicted signal. By using CCSWD, we increase this correlation and therefore improve the localization resolution. Figure 10 illustrates the localization of two holes in the middle of the plate using CCSWS integrated with MFP

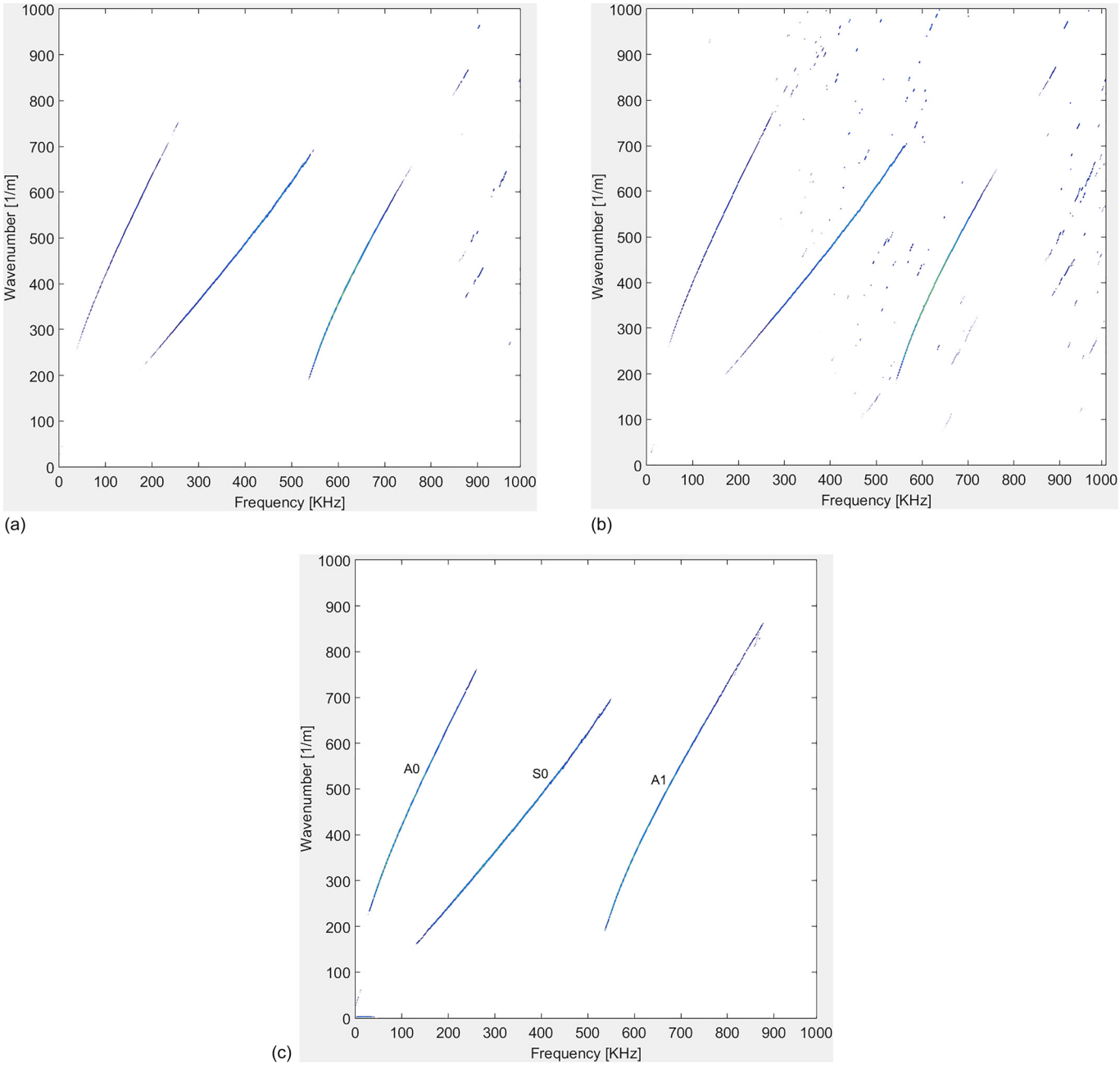

FIG. 9. (Color online) Dispersion curves reconstructed by (a) BPSWA, (b) OMP, and (c) CCSWA using experimental data with 1 MHz bandwidth.

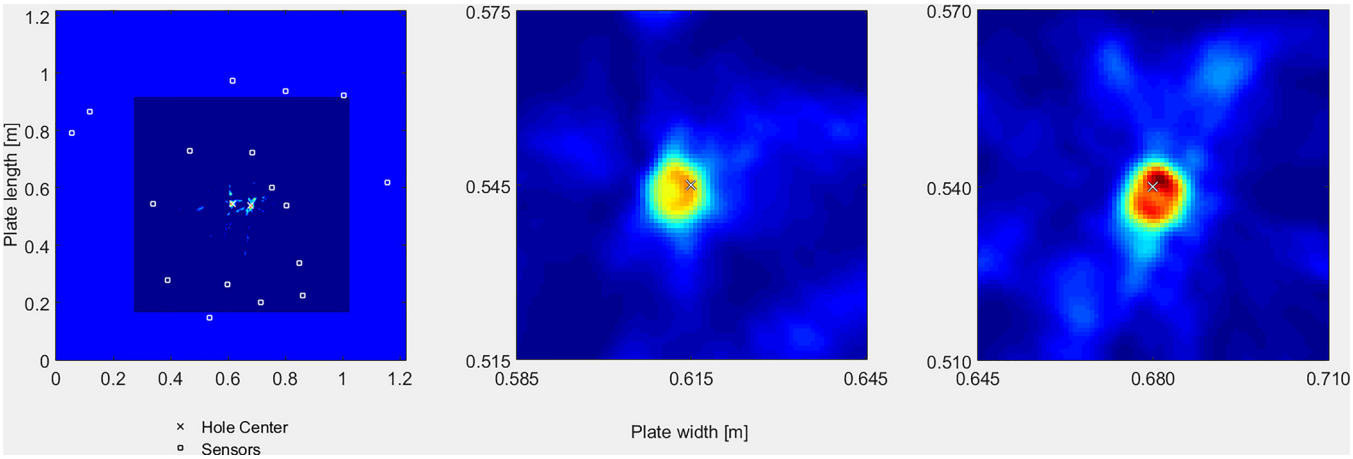

FIG. 10. (Color online) Localization of two scatters in middle of the metal plate using CCMFP with experimental data. The brightness at different locations represents the correlation strength between the measured signals and the predicted signals.

(CCMFP). The brightness at different locations represents correlation values. Figure 10 shows that CCMFP localizes the two scatterers successfully, as indicated by the two bright spots where the correlation between the measured signal and the predicted signal peaks. Further, in the zoomed-in figures, we see that CCMFP achieves good localization resolution. We use the peak-to-sidelobe ratio[57] (PSR) to measure the peak sharpness in the matched field processing output

$$PSR = \frac{\text{peak} - \mu}{\sigma}, \tag{17}$$

where peak is the maximum correlation value in Fig. 10. Symbols μ and σ denote the mean and standard deviation of a 20×20 sidelobe region excluding a 5×5 central mask region centered at the peak. The higher the PSR, the sharper the peak compared with the sidelobe and the higher the localization resolution. Table IV shows the PSR of CCMFP, MFP using basis pursuit (BMFP), and MFP using orthogonal matching pursuit (OMFP), respectively. The table shows that CCMFP achieves the highest correlation value at the peak while the mean and standard deviation of the sidelobes are roughly the same. As a result, CCMFP has the highest PSR.

Overall, the proposed CCSWA algorithm demonstrates better results than SWA and OMP with respect to the accuracy in dispersion curves reconstruction, signal synthesis, and damage localization.

IV. CONCLUSIONS

This paper addresses the discontinuity problem exhibited by SWA[8] when reconstructing the dispersion curves of Lamb waves. We develop a continuity constrained sparse wavenumber analysis method to reconstruct dispersion curves of Lamb waves propagating in a metal plate. In contrast with two other sparse reconstruction methods, one using basis pursuit[8] and the other using orthogonal matching pursuit,[10,30–32] the CCSWA accounts for frequency continuity in the sparse frequency-wavenumber representation of Lamb waves by adding a weighted penalty to the l_1 regularization term in the original *LASSO* optimization problem. This better models Lamb wave propagation. With a set of carefully designed procedures, the CCSWA promotes continuity constrained sparse reconstruction, resulting in smooth, continuous, and clean dispersion curves as demonstrated both with simulation and experimental data. CCSWA improves the results of signal denoising and signal synthesis as shown by the increase in the value of the correlation coefficients between the synthesized signals and the true signals. With CCSWA, we can reduce the number of measurements by 80% and still obtain performance comparable to the original SWA[8] as demonstrated with experimental data. CCSWA combined with matched field processing also improves the localization performance by increasing the peak-to-sidelobe ratio from an image of two holes in a plate.

In future work, we will utilize a probabilistic framework for averaging weights, rather than the deterministic weight-assigning method described here. Different processors, such as the linear cross correlator (Bartlett) processor, maximum likelihood processor,[28,58] cross-frequency incoherent processor, pair-wise processor, and coherent normalized processor[59] can also be used to achieve better localization.

TABLE IV. Peak-to-sidelobe ratio of the matched field processing output with CCMFP, BMFP, and OMFP, respectively. Symbols μ and σ are the mean and standard deviation of the sidelobe.

	Peak	μ	σ	PSR
CCMFP	10.05	0.06	0.14	71.36
BMFP	9.80	0.06	0.14	69.57
OMFP	8.97	0.05	0.13	68.62

ACKNOWLEDGMENTS

This research was funded in part by the National Natural Science Foundation of China (61401524), Natural Science Foundation of Guangdong Province (2014A030313123), Natural Science Foundation of Guangzhou City (201605121423270), the Fundamental Research Funds for the Central Universities (15lgjc10), and National Key Research and Development Program (2016YFC0103905). This material is based upon work supported by the National Science Foundation

under Grant No. CMMI-1562838. The work of Y.J. was supported in part by the National Science Foundation under Grant No. CMMI-1126008.

[1]J. Achenbach, *Wave Propagation in Elastic Solids*, edited by J. D. Achenbach (Elsevier, Amsterdam, 1975), Chap. 6, pp. 202–261.
[2]D. N. Alleyne, "The nondestructive testing of plates using Lamb waves," Ph.D. dissertation, Mechanical Engineering Department, Imperial College of London, London (1991).
[3]B. Sorazu, B. Culshaw, and G. Thursby, "Obtaining complementary Lamb wave dispersion information by two signal processing methods on an all-optical non-contact configuration," Sens. Actuators A **217**, 95–104 (2014).
[4]T. Hayashi, W. J. Song, and J. L. Rose, "Guided wave dispersion curves for a bar with an arbitrary cross-section, a rod and rail example," Ultrasonics **41**, 175–183 (2003).
[5]A. Raghavan and C. E. S. Cesnik, "Guided-wave signal processing using chirplet matching pursuits and mode correlation for structural health monitoring," Smart Mater. Struct. **16**(2), 61741B (2007).
[6]L. Draudvilienė, R. Raišutis, E. Žukauskas, and A. Jankauskas, "Validation of dispersion curve reconstruction techniques for the *A*0 and *S*0 modes of Lamb waves," Int. J. Struct. Stab. Dyn. **14**, 14–24 (2014).
[7]S. Hedayatrasa, T. Q. Bui, C. Zhang, and C. W. Lim, "Numerical modeling of wave propagation in functionally graded materials using time-domain spectral Chebyshev elements," J. Comput. Phys. **258**, 381–404 (2014).
[8]J. B. Harley and J. M. F. Moura, "Sparse recovery of the multimodal and dispersive characteristics of Lamb waves," J. Acoust. Soc. Am. **133**, 2732–2745 (2013).
[9]J. B. Harley and J. M. F. Moura, "Data-driven matched field processing for Lamb wave structural health monitoring," J. Acoust. Soc. Am. **135**(3), 1231–1244 (2014).
[10]J. B. Harley and J. M. F. Moura, "Dispersion curve recovery with orthogonal matching pursuit," J. Acoust. Soc. Am. **137**(1), EL1–EL7 (2015).
[11]W. Gao, G. Christ, and T. Jan, "Laser ultrasonic study of Lamb waves: Determination of the thickness and velocities of a thin plate," Int. J. Eng. Sci. **41**(2), 219–228 (2003).
[12]S. Pant, J. Laliberte, M. Martinez, and B. Rocha, "Derivation and experimental validation of Lamb wave equations for an n-layered anisotropic composite laminate," Compos Struct. **111**, 566–579 (2014).
[13]S. Pant, J. Laliberte, M. Martinez, B. Rocha, and D. Ancrum, "Effects of composite lamina properties on fundamental Lamb wave mode dispersion characteristics," Compos Struct. **124**, 236–252 (2015).
[14]P. Packo, T. Uhl, and W. J. Staszewski, "Generalized semi-analytical finite difference method for dispersion curves calculation and numerical dispersion analysis for Lamb waves," J. Acoust. Soc. Am. **136**, 993–1002 (2014).
[15]S. Sorohan, N. Constantin, M. Găvan, and V. Anghel, "Extraction of dispersion curves for waves propagating in free complex waveguides by standard finite element codes," Ultrasonics **51**, 503–515 (2010).
[16]R. K. Singh, C. Ramadas, R. D. Misal, and D. G. Thakur, "Numerical analysis of Lamb wave propagation in delaminated composite laminate," Int. Conf. Modell. Opt. Comput. **38**, 2510–2519 (2012).
[17]L. Ambrozinski, P. Packo, L. Pieczonka, T. Stepinski, T. Uhl, and W. J. Staszewski, "Identification of material properties—Efficient modelling approach based on guided wave propagation and spatial multiple signal classification," Struct. Control. Hlth. **22**, 969–983 (2015).
[18]H. Gravenkamp, C. Birk, and C. Song, "Numerical modeling of elastic waveguides coupled to infinite fluid media using exact boundary conditions," Comput. Struct. **141**, 36–45 (2014).
[19]H. Gravenkamp, F. Bause, and C. Song, "On the computation of dispersion curves for axisymmetric elastic waveguides using the scaled boundary finite element method," Comput. Struct. **131**, 46–55 (2014).
[20]E. Bossy and Q. Grimal, "Numerical methods for ultrasonic bone characterization," in *Bone Quantitative Ultrasound*, edited by L. Pascal and H. Guillaume (Springer, Amsterdam, 2011), Chap. 8, pp. 181–228.
[21]C. Sbarufatti, G. Manson, and K. Worden, "A numerically-enhanced machine learning approach to damage diagnosis using a Lamb wave sensing network," J. Sound Vib. **333**, 4499–4525 (2014).
[22]S. Agarwal and M. Mitra, "Lamb wave based automatic damage detection using matching pursuit and machine learning," Smart Mater. Struct. **23**, 085012 (2014).
[23]S. Agarwal and M. Mitra, "Lamb wave based damage detection using matching pursuit and support vector machine classifier," Proc. SPIE Int. Soc. Opt. Eng. **9064**, 11–25 (2014).
[24]K. Sun, K. Hong, L. Yuan, Z. Shen, and X. Ni, "Inversion of functional graded materials elastic properties from ultrasonic Lamb wave phase velocity data using genetic algorithm," J. Nondestruct. Eval. **33**, 34–42 (2014).
[25]Y. Ying, J. Harley, J. H. Garrett, Jr., Y. Jin, I. J. Oppenheim, J. Shi, and L. Soibelman, "Applications of machine learning in pipeline monitoring," Proc. Comput. Civil Eng. 242–249 (2011).
[26]B. Liu, L. Tang, J. Wang, A. Li, and Y. Hao, "2-D defect profile reconstruction from ultrasonic guided wave signals based on QGA-kernelized ELM," Neurocomputing **128**, 217–223 (2014).
[27]Z. Tian and L. Yu, "Lamb wave frequency-wavenumber analysis and decomposition," J. Intel. Mater. Syst. Str. **25**, 1107–1123 (2014).
[28]A. B. Baggeroer, W. A. Kuperman, and P. N. Mikhalevsky, "An overview of matched field methods in ocean acoustics," IEEE J. Oceanic Eng. **18**, 401–424 (1993).
[29]J. B. Harley, A. C. Schmidt, and J. M. F. Moura, "Accurate sparse recovery of guided wave characteristics for structural health monitoring," in *2012 IEEE International Ultrasonics Symposium* (2012), pp. 158–161.
[30]J. A. Tropp, "Just relax: Convex programming methods for identifying sparse signals in noise," IEEE Trans. Inf. Theory. **52**, 1030–1051 (2006).
[31]J. A. Tropp and A. C. Gilbert, "Signal recovery from random measurements via orthogonal matching pursuit," IEEE Trans. Inf. Theory. **53**, 4655–4666 (2007).
[32]Y. C. Pati, R. Rezaiifar, and P. S. Krishnaprasad, "Orthogonal matching pursuit: Recursive function approximation with applications to wavelet decomposition," in *IEEE Proceedings of The Twenty-Seventh Asilomar Conference on Signals, Systems and Computers* (1993), Vol. 1, pp. 40–44.
[33]K. F. Graff, *Wave Motion in Elastic Solids* (Ohio State University Press, Columbus, OH, 1975), Chap. 8, pp. 431–579.
[34]K. Han, Y. Wang, B. Kou, and W. Hong, "Parameters estimation using a random linear array and compressed sensing," in *2010 3rd International Congress on Image and Signal Processing* (2010), pp. 3950–3954.
[35]D. L. Donoho, "Compressed sensing," IEEE Trans. Inf. Theory. **52**, 1289–1306 (2006).
[36]D. L. Donoho, M. Elad, and V. N. Temlyakov, "Stable recovery of sparse overcomplete representations in the presence of noise," IEEE Trans. Inform. Theory. **52**, 6–18 (2006).
[37]M. A. Davenport, M. F. Duarte, Y. C. Eldar, and G. Kutyniok, "Introduction to compressed sensing," in *Introduction to Compressed Sensing: Theory and Applications*, edited by Y. C. Eldar and G. Kutyniok (Cambridge University Press, New York, 2012), pp. 1–64.
[38]M. A. T. Figueiredo, R. D. Nowak, and S. J. Wright, "Gradient projection for sparse reconstruction: Application to compressed sensing and other inverse problems," IEEE J. Sel. Top. Sign. **1**, 586–597 (2007).
[39]E. J. Candes and M. B. Wakin, "An introduction to compressive sampling," IEEE Sign. Proc. Mag. **25**, 21–30 (2008).
[40]B. Rajaratnam, S. Roberts, D. Sparks, and O. Dalal, "Lasso regression: Estimation and shrinkage via the limit of Gibbs sampling," J. R. Stat Soc. B **78**(1), 254–259 (2015).
[41]J. D. Blanchard, C. Cartis, and J. Tanner, "Compressed sensing: How sharp is the restricted isometry property?," SIAM Rev. **53**, 105–125 (2011).
[42]S. Kunis and H. Rauhut, "Random sampling of sparse trigonometric polynomials. II. Orthogonal matching pursuit versus basis pursuit," Found. Comput. Math. **8**, 737–763 (2008).
[43]J. J. Fuchs, "Recovery of exact sparse representations in the presence of bounded noise," IEEE Trans. Inform. Theory **51**, 3601–3608 (2005).
[44]S. Irvin, "An isotropic 3×3 image gradient operator," in *Machine Vision for Three-dimensional Sciences* (1990), pp. 1–5.
[45]C. M. Bishop, *Pattern Recognition and Machine Learning* (Springer, New York, 2006), Chap. 10, pp. 462–486.
[46]A. Corduneanu and C. M. Bishop, "Variational Bayesian model selection for mixture distributions," in *Proceedings of the Eighth International Conference on Artificial Intelligence and Statistics* (Morgan Kaufmann, San Francisco, CA, 2001), pp. 27–34.
[47]T. P. Centeno and N. D. Lawrence, "Optimising kernel parameters and regularisation coefficients for non-linear discriminant analysis," J. Mach. Learn. Res. **7**, 455–491 (2006).
[48]S. Subedi and P. D. McNicholas, "Variational Bayes approximations for clustering via mixtures of normal inverse Gaussian distributions," Adv. Data Anal. Class. **8**, 167–193 (2014).

[49]J. B. Harley and J. M. F. Mourn, "Matched field processing localization with random sensor topologies," in *2014 IEEE International Conference on Acoustics, Speech and Signal Processing* (2014), pp. 1404–1408.
[50]P. R. Gill, A. Wang, and A. Molnar, "The in-crowd algorithm for fast basis pursuit denoising," IEEE Trans. Sign. Process. **59**(10), 4595–4605 (2011).
[51]D. M. Malioutov, C. Müjdat, and A. S. Willsky, "Homotopy continuation for sparse signal representation," in *Proceedings of Acoustics, Speech, and Signal Processing, 2005* (2005), Vol. 5, pp. 733–736.
[52]M. D. Gilchrist, "Attenuation of ultrasonic Rayleigh–Lamb waves by small horizontal defects in thin aluminium plates," Int. J. Mech. Sci. **41**, 581–594 (1999).
[53]J. B. Harley, C. Liu, I. J. Oppenheim, D. W. Greve, and J. M. F. Moura, "Coherent, data-driven Lamb wave localization under environmental variations," AIP Conf. Proc. **1650**, 202–210 (2015).
[54]C. Liu, J. Harley, N. ODonoughue, Y. Ying, M. H. Altschul, M. Berges, J. H. Garrett, D. W. Greve, J. M. F. Moura, I. J. Oppenheim, and L. Soibelman, "Robust change detection in highly dynamic guided wave signals with singular value decomposition," in *2012 IEEE International Ultrasonics Symposium* (2012), pp. 483–486.
[55]C. Liu, J. B. Harley, M. Bergés, D. W. Greve, W. R. Junker, and I. J. Oppenheim, "A robust baseline removal method for guided wave damage localization," Proc. SPIE **9061**, 15–19 (2014).
[56]J. D. Tippmann, X. Zhu, and F. L. di Scalea, "Application of damage detection methods using passive reconstruction of impulse response functions," Philos. Trans. R. Soc. London Ser. A **373**, 447–453 (2015).
[57]M. Savvides, B. V. K. Kumar, and P. Khosla, "Face verification using correlation filters," in *3rd IEEE Automatic Identification Advanced Technologies* (2002), pp. 56–61.
[58]K. Yang and Y. Ma, "Matched field processing in a mismatch and multi-source environment," in *2005 IEEE Proceedings of Oceans* (2005), Vol. 2, pp. 1181–1186.
[59]S. E. Dosso and M. J. Wilmut, "Maximum-likelihood and other processors for incoherent and coherent matched-field localization," J. Acoust. Soc. Am. **132**, 2273–2285 (2012).